



# Measurement and Investigation on the Jet Interface Structure

C. Gong<sup>1†</sup>, M. G. Yang<sup>1</sup> and W. D. Jia<sup>2</sup>

<sup>1</sup> School of Energy and Power Engineering, Jiangsu University 1, Zhenjiang, Jiangsu, 212013, China

<sup>2</sup> Key Laboratory of Modern Agricultural Equipment and Technology, Jiangsu University 2, Zhenjiang, Jiangsu, 212013, China

†Corresponding Author Email: [chengong@ujs.edu.cn](mailto:chengong@ujs.edu.cn)

(Received April 17, 2017; accepted July 19, 2017)

## ABSTRACT

The well understanding of interface structure of liquid jet is the basis of the research of primary breakup. In this paper, the interface structure of liquid jet is captured by using a high-speed photography. The key parameters of interface structure, streamwise wavelength, spanwise wavelength and generation position, are measured based on a power spectral method. The results show that jet interface is featured by a group of periodic structures in the region near the nozzle exit. The position where periodic structure generated fluctuates in a certain region with the variation of time and spanwise position. The spanwise wavelength of these periodic structures is the function of nozzle diameter and the wavelength increase ratio of transition region. Along the streamwise direction, the streamwise wavelengths of these structures increase with a small ratio. With the Weber number increase, the streamwise wavelength is significantly decreased while the spanwise wavelength has no remarkable change. A Reynolds number that defined with streamwise distance, jet velocity and viscosity is proposed to estimate the onset of interface structure, and Reynolds number is equal to 42000 in this paper.

**Keywords:** Liquid jet; Interface structure; Wavelength; Transition position.

## 1. INTRODUCTION

The atomization of liquid jet has an extensive technological application in agriculture and industry, like fertilizer spraying and fuel injection (Lefebvre 1998; Tryggvason 2000). The primary breakup that introduced by the development of jet interface structures is supposed to play an important role in atomization process (Joseph *et al.* 1999; Julien *et al.* 2011). Therefore, the interface structures of the liquid jet should be studied firstly before the atomization can be well understood.

Generally, most of researches believed that the development of shear layer has an important effect on the deformation of jet interface. Various theories were proposed to explain the reason responsible for the generation of jet interface structures. Some of them believe that aerodynamic effect on the interfacial instability plays an important role on the deformation of jet interface. (Lasheras *et al.* 2000; Yecko, *et al.* 2002, 2005; Marmottan *et al.* 2004; Eggers *et al.* 2008; Gorokhovski *et al.* 2008; Shinjo *et al.* 2010, 2011).

In their works, the Kelvin-Helmholtz instability that introduced by the velocity different between liquid and gas phase is applied to describe the formation and development of jet interface structures. Meanwhile, there are also researchers indicate that the shear layer instability inside the liquid shear layer dominate the development of the jet interface structures (Wu *et al.* 1995; Yoon *et al.* (2003, 2004); Park & Heister 2006; Umemura *et al.* 2011, 2014). They proposed that the relaxation of velocity profile and the generation of inflection point of velocity profile may introduce rollup motion and lead to interface deformation. The release of surface energy produce capillary wave, which transfer energy upstream and makes a further effect on the jet interface structures. The aforementioned works proved instructive guidance for the research of this field. The further investigations may provide deep understanding on the interface structures of the liquid jet.

To some extent, the study of the interface structures is depended on the well captured information of these structures. Generally, they can be captured by either numerical simulation method or visualization

experimental method. Some researchers attempt to investigate the interface structure by using Direct Numerical Simulation (Shinjo *et al.* 2010, 2011a, b; Cousin *et al.* 2012; Desjardins *et al.* 2013; Mehravaran *et al.* 2013; Behzad *et al.* 2016) and Large Eddy Simulation (Xiao *et al.* 2014, 2016; Tian *et al.* 2015; Ghiji *et al.* 2016). Based on the accurate boundary condition, the interface structure of liquid jet can be well reproduced by these methods. The accurate boundary conditions are usually measured by experimental methods.

In the aspect of experiment, pulsed photography, flash photography, holography and pulsed shadowgraph photography are common used method in the early time. Wu *et al.* (1992, 1993, 1995), Faeth *et al.* (1995) and Sallam *et al.* (1999, 2002) conducted a series of representative works on the interface structure of the liquid jet based on these methods. The effects, such as aerodynamic, initial flow condition and density ratio on the development of the interface structure were discussed. With the development of experimental techniques, some advanced methods are used. By using an X-ray imaging method, the interface structure was investigated by Osta *et al.* (2012). A microscopy technique was developed by Reddemann *et al.* (2013) to capture the micro-scale structure of liquid jet. The interface structures of air-assisted water jets were studied by Zhao *et al.* (2014, 2015) with a high-speed photography. With the help of a high-speed visualization method, the temporal evolution of ligament is captured and measured by Dumouchel *et al.* (2015). The optical connectivity, electrical connectivity and shadowgraphy were used in Charalampous's work (Charalampous *et al.* 2016) to investigate the interface structure of liquid jet. A high-speed microscopic photography is used in Kourmatzis's experiment (Kourmatzis *et al.* 2016) to investigate the interface structures of effervescent and air-blast jet. In Abderrezzak's work (Abderrezzak *et al.* 2016), the cavitation inside the nozzle and the jet interface structures near the nozzle are recorded with a high-speed visualization system. The relationship between cavitation and jet interface structures is discussed. High-speed shadowgraphy technique is used in Jadidi's work (Jadidi *et al.* 2016) to study the interface structure of water jets in transverse free air jets. The development of jet interface structures are recorded and discussed by Wang (Wang *et al.* 2016) with a high-speed microscopic photography. The aforementioned works served as a methodology basis for further research work.

In this paper, the jet interface structures in both streamwise and spanwise direction are well captured with a high-speed photomicrography. The parameters of the interface structure, streamwise wavelength, spanwise wavelength, and generation position, are measured with an innovative image processing method. The highest velocity of the jet that produces in our experiment is around 40 m/s and the corresponding Reynolds number is equal to  $1.1 \times 10^5$ . Furthermore, the effect of the Weber number on these parameters is discussed.

## 2. EXPERIMENTAL APPROACH

### 2.1 Experiment Setup

The experimental system consists of two parts: jet generating device and high speed imaging system. The jet generating device includes pump, variable-frequency drive, pipe and nozzle. As shown in Fig. 1(a), water is pumped from a container, and then enters a straight stainless steel pipe via a rubber hose. The length and inner diameter of the pipe are 500 mm and 8 mm, respectively. There is no bend at the pipe inlet and the length-to-diameter ratio of the pipe exceeds 40, which ensures fully developed pipe flow (Faeth *et al.* 1995; Mayer *et al.* 2004). Finally, the pipe flow passes through the nozzle and the jet is generated. A variable-frequency drive is used to control the flow rate of the pump, which determines the jet velocity. The configuration of the copper nozzle is presented in Fig. 1(b). The outlet diameters  $D$  and inlet diameter  $d$  of nozzle are equal to 3 mm and 8 mm, respectively. The contraction angle  $\theta_1$  of the nozzle is  $10^\circ$ .

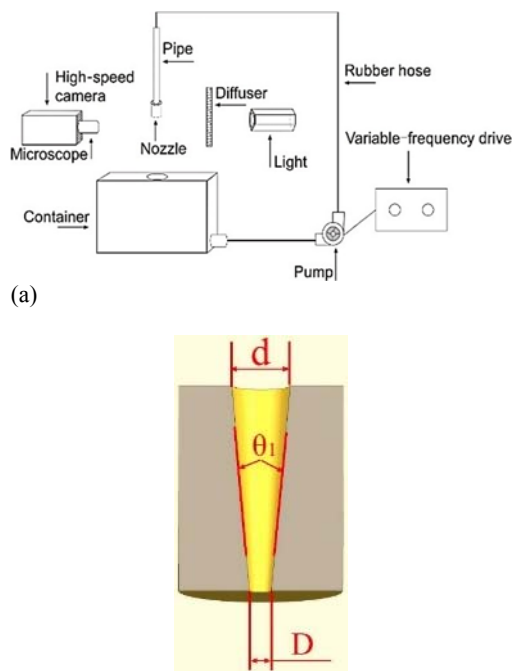


**Fig. 1. (a) Experimental setup. (b) Nozzle configuration.**

As presented in Fig. 2(a), the jet interface wave is generated at a distance downstream the nozzle exit. Near the nozzle exit, the jet interface is fairly smooth. If the interface waves are introduced by surface roughness of the pipe and nozzle, they should appear at the nozzle exit immediately. Therefore, the surface roughness of the pipe and nozzle is small enough and has little effect on jet interface structures. Moreover, the surface roughness depends on processing techniques and material properties, which are beyond the concern of this paper.

There may be some pressure fluctuation produced by the pump. However, water flow enters the stainless steel pipe via a rubber hose, whose length is long enough to reduce the energy of the pressure fluctuation to a low level. Furthermore, Meier's work (Meier *et al.* 1992) show that the scale of wave that produced by pressure fluctuation is bigger than nozzle diameter. As shown in Fig. 2(a), in our experiment, the scale of surface wave is obviously smaller than the nozzle diameter. Therefore, the pressure fluctuation has little effect on the jet interface structures.

A high speed imaging system is used to capture the interface structure of the liquid jet. It includes high-speed camera (OLYMPUS I-SPEED 3), microscope, diffuser and light source (OLYMPUS ILP-2). The microscope is used to amplify the micro-scale interface structure. The amplification of the microscope is set as 2.8 which provide typical resolution around 6 μm /pixel. The exposure time and the frame rate of the camera were set as 1 μs and 2000 fps respectively. In this case, the image size is 1280×1024 pixels. The light beam passes through a 5 mm thickness acrylic diffuser plate before touching the jet. The acrylic diffuser plate is used to produce a uniform light distribution.

The average velocity of the liquid jet core near the nozzle exit is measured in our experiments. The average jet velocity was also used in some relevant research (Hoyt & Taylor (1977a, b)). In our experiments, the nozzle diameter is only 3 mm, and the maximum velocity of the jet is around 40 m/s. Based on Eq. (1) (Pohlhausen 1921), the boundary layer thickness is around 0.1 mm. The velocity gradients within this boundary layer are difficult to measure with existing experimental installation.

$$\delta = \frac{3}{2\sin\theta} \sqrt{\frac{2D\nu}{U}} \quad (1)$$

where δ is the boundary layer thickness, θ is the angle of the converging nozzle, D is the diameter of the nozzle exit, ν is the kinematic viscosity, U is the jet velocity.

The PIV is used to measure the jet velocity. The PIV technique represents a non-intrusive measurement technique that will not disturb the flow near the nozzle exit. The PIV system consists of a Flow Sense EO-Dual Power pulsed laser, a Flow Sense EO 2M CCD camera and a microscope. The initial section (near the nozzle exit) of the jet is focused. In order to reduce the random error, several groups of data were acquired under the same experimental condition. The average of these data was set as the final average jet velocity. Based upon the literature (Bian *et al.* 2010; Syuto *et al.* 2010; Hori & Sakakibara 2004), the uncertainty of velocity measurement with PIV is less than 3% with a confidence level of 95%.

Water temperature is measured by using a WS-T11PRO digital thermometer. The density, viscosity and surface tension are estimated accordingly. The accuracy of the digital thermometer is ±0.5°C. The flow parameters are presented in the Table 1.

**Table 1 Flow parameters**

Parameter	Value
Liquid temperature T	293±0.5 K
Liquid density ρ <sub>L</sub>	998 kg/m <sup>3</sup>
Ambient pressure P	0.1 MPa
Air density ρ <sub>g</sub>	1.21 kg/m <sup>3</sup>
Surface tension σ	0.07275 N/m
Kinematic viscosity ν	1.007×10 <sup>-6</sup> m <sup>2</sup> /s

A series of experiments were conducted under the different inlet pressures. The velocities of these jets were measured. The Weber number  $We_g$  that based on air density and Reynolds number  $Re$  are calculated:

$$Re = \frac{UD}{\nu}, We_g = \frac{\rho_g U^2 D}{\sigma} \quad (2)$$

Where ρ<sub>g</sub> is the air density, σ is the surface tension.

The velocities, Reynolds numbers and the Weber numbers are presented in Table 2.

**Table 2 Jet velocities, Reynolds numbers and Weber numbers**

Case	velocity	Re	We <sub>g</sub>
a	12.6	3.4 × 10 <sup>4</sup>	8.0
b	16.7	4.6 × 10 <sup>4</sup>	13.9
c	20.6	5.6 × 10 <sup>4</sup>	21.1
d	25.3	6.9 × 10 <sup>4</sup>	32.0
e	28.0	7.6 × 10 <sup>4</sup>	39.2
f	32.3	8.8 × 10 <sup>4</sup>	51.9
g	36.8	1.0 × 10 <sup>5</sup>	67.6
h	40.4	1.1 × 10 <sup>5</sup>	81.3

## 2.2 Image Processing Method

### 2.2.1 Measurement of Streamwise Wavelength and Onset Position of Interface Structure

In this part, the image processing method is discussed. The basic idea of the image processing method is to obtain the quantitative information by processing the image intensities that extract from the jet images. Fig. 2(a) is one of the jet images that captured in our experiments. As it presented in the image, the jet surface is smooth and there is no clear structure in the region of X/D=0~1. Then, a group of periodic wave-like structures appears on the jet surface in the region of X/D=1~1.7. The streamwise distance between two adjacent waves is equal to 0.1 D, which means the wavelength of the interface structure is equal to 0.1 D. The image intensities that extracts from the red line of Fig. 2(a) is plotted in the Fig. 2(b). The distribution of the image intensities is similar with sinusoidal distribution, and the distance between two adjacent crests is around 0.1 D. With this in mind, it is easy to find that the wavelength can

get by measuring the periodicity of the image intensities.

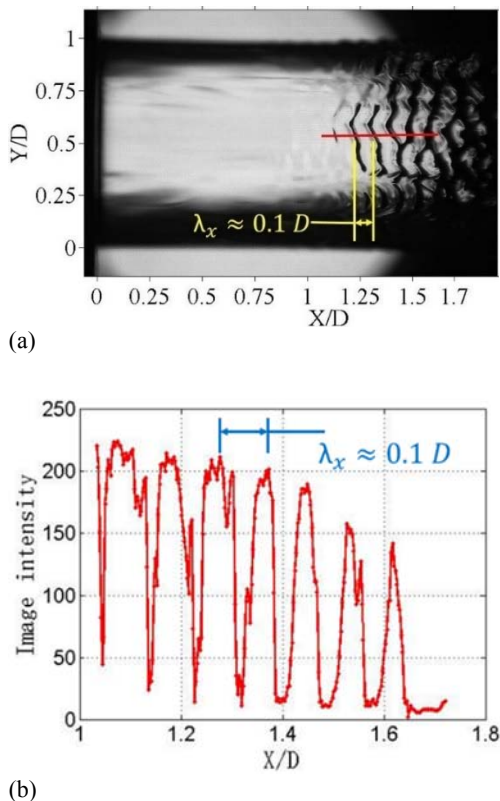


**Fig. 2. (a) Jet image. The jet ejects from left to right. X direction is the streamwise direction, Y direction is the spanwise direction. X/D=0 is corresponding to the nozzle exit. (b) Curve of image intensities.**

Spectrum analysis is a common used method to analyze the periodicity of digital signal. Therefore, one of the spectrum analysis methods, Welch method, is used here to process the image intensities. In order to highlight the main lobe signal and suppress the side lobe signal, the Blackmann window is selected in the Welch method (Mulgrew 2002). According to the principle of the Welch method, the sample should at least contain multiple sine waves so as to give the accurately result. Therefore the length of the sample is set as 0.5 D, which is corresponding to 260 pixels. In order to obtain the variation of the wavelength, a series of measurements were performed along the streamwise direction. The first sample is taken from the exit of the nozzle and the measured result is set as the wavelength of the middle point of this sample. Then the second sample was taken from the position of 0.02 D, approximately 11 pixels, downstream of the nozzle exit. The procedure was repeated until the end of the data set.

The wavelengths of different spanwise positions and times are measured since the jet is turbulence flow. The three wavelengths curves in Fig. 3(b) are the measured results of the three different spanwise positions (Y positions) which are indicated with red, blue and yellow lines in Fig. 3(a). Similarly, the

three wavelengths curves in Fig. 4(d) are the measured results of the three different times that are shown in Figs. 4(a), (b) and (c). The jets of Figs. 4(a), (b) and (c) are under the same experimental condition but different times.

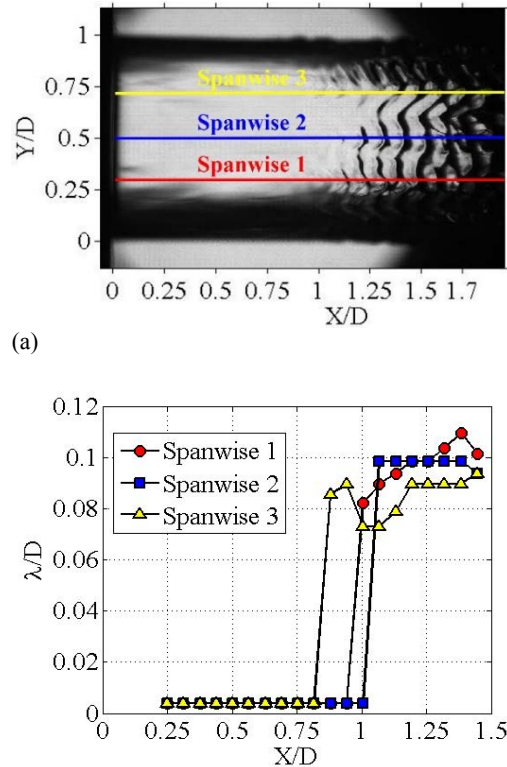


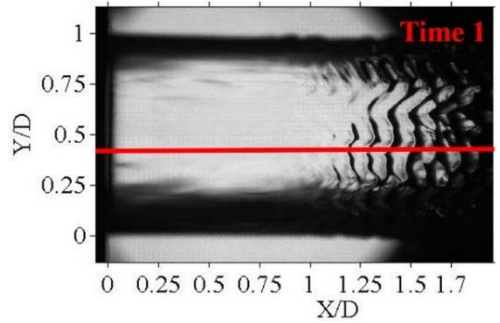
**Fig. 3. (a) Jet image. Red, blue and yellow lines indicate three different spanwise positions. (b) Variation of wavelengths with different spanwise positions.**

Figures 3 and 4 are not only used to show that measured wavelengths vary with time and spanwise position, but also used to explain the reason why there is a Zone 2 in the average results (Fig. 5). The detailed explanation is presented as follow.

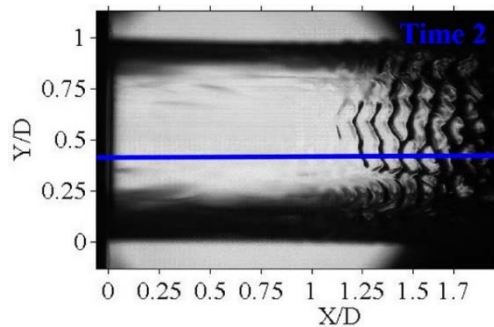
In order to obtain the general rule of the wavelength and reduce the random error, 100 images of different times and 100 spanwise positions of each image are measured. The average wavelength of 10000 sets of data is presented in the Fig. 5. The average result consists of three zones. Zone 1 and Zone 3 are corresponding to the smooth and unsmooth part of the jet surface respectively. The streamwise wavelength  $\lambda_x$  of the interface structure is equal to the wavelength of Zone 3. In the Zone 2, the jet surface is either smooth or unsmooth. Therefore, this Zone is defined as transition Zone. The generation positions of the interface structure are located in the region of transition Zone.

The exit of Zone 2 is due to the average. As shown in Fig. 3(b) and Fig. 4(d), for the single measured result, the position where wavelength dramatically increases (corresponding to the position where jet interface translates from smooth part to non-smooth

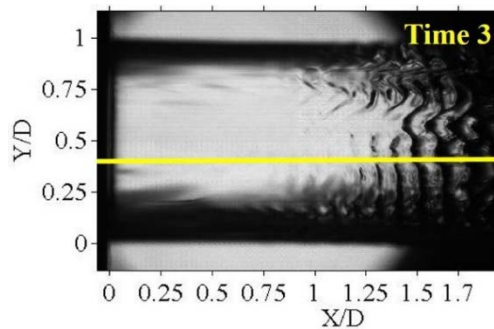
part) is a “point of streamwise position”. It fluctuates in a certain streamwise range. This streamwise range is corresponding to the Zone 2 of the average result in Fig. 5.



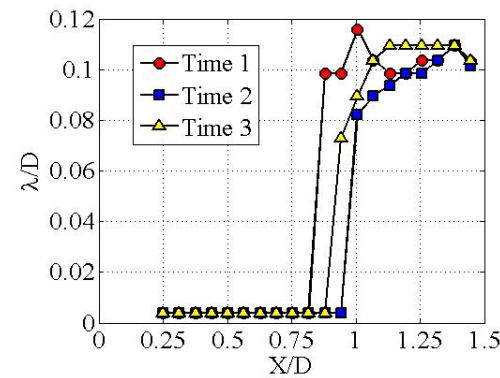
(a)



(b)



(c)



(d)

**Fig. 4.** (a), (b) and (c) are the jet images of the same experimental conditions but different times. (d) Variation of wavelength with different time.

The Zone 2 can be used to estimate the position where jet interface translates from smooth to non-smooth and the transition probability of jet interface. As it shown in Fig. 5, the positions where jet interface translates from smooth part to non-smooth part are limited within the range of  $X/D=0.8\sim 1.15$ . Meanwhile, the bigger the wavelength in Zone 2, the more probability the jet interface translates from smooth part to non-smooth part.

In the Zone 3 of Fig. 5, the increase of wavelengths is due to the acceleration of jet interface and the relaxation of the velocity profile of the liquid jet. The researches of Goldstein (Goldstein S 1933), Sato (Sato & Kuriki 1961) and Brennen (Brennen C 1970) show that the jet interface flow is similar to that in the wake of a thin flat plate, and the flow on jet interface accelerates near the nozzle exit. It produces a positive axial strain rate, which stretches fluid elements in the streamwise direction and thus enlarges the wavelengths.

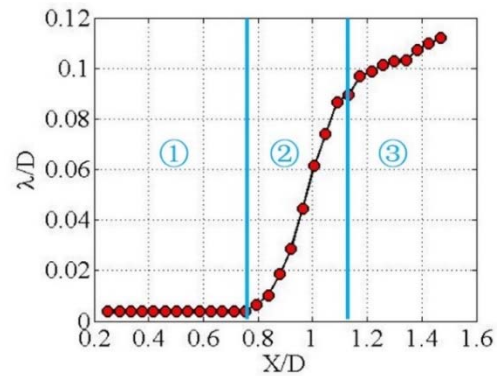


**Fig. 5.** Variation of average wavelengths.

### 2.2.2 Measurement of Spanwise Wavelength of Interface Structure

As it shown in the Fig. 6, along the spanwise direction, the distribution of the interface structure is similar with sinusoidal distribution. The distance between two adjacent wave crests is the spanwise wavelength  $\lambda_y$ . It is easy to find that the spanwise wavelength is equal to twice of the curvature radius of the interface structure. Therefore, the spanwise wavelength can be obtained by measuring the curvature radius of the interface structure.

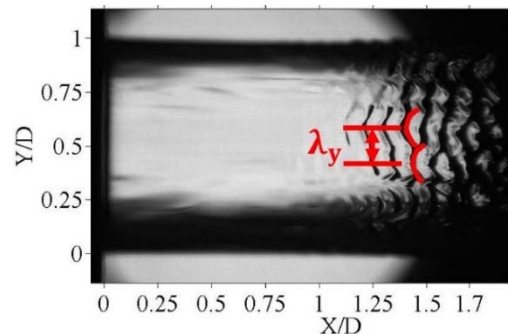


**Fig. 6** Spanwise wavelength of interface structure.

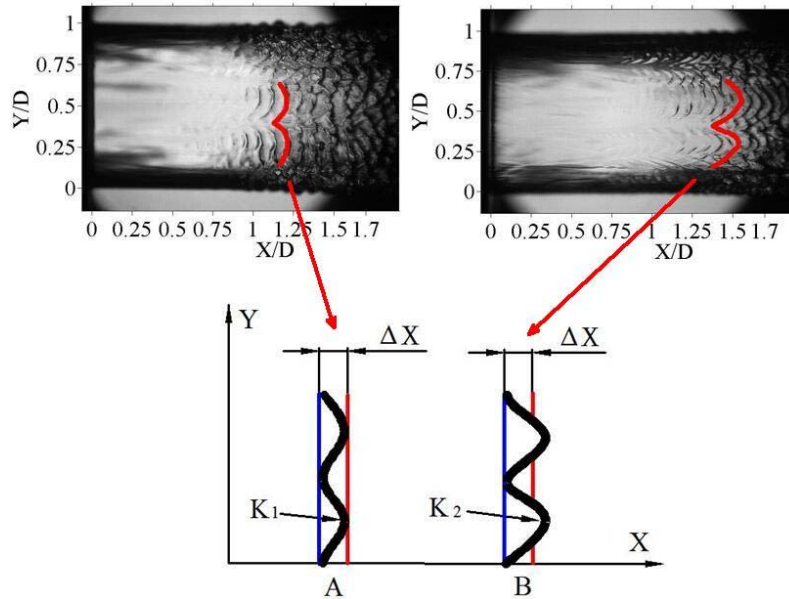


**Fig. 7. The curvature radius of different interface structures.  $K_1$  and  $K_2$  are the curvatures of A and B.**

The curvature radius of the interface structure can be estimated by the wavelength increase ratio of transition Zone of Fig. 5. The relationship between wavelength increase ratio and curvature radius is discussed here.

As it presented in Fig. 7, two wavy lines that have different curvature radius were used to demonstrate the interface structures. These wavy lines are named as A and B. As it mentioned above, the sample will move downstream with a certain distance after each measurement. Here, the distance is assumed equal to  $\Delta X$ . The spanwise distance where sample can reach the wavy line will increase after the samples moves from the position of blue line to the position of red line. As it plotted with red lines, for A, at all spanwise positions, the sample can reach the wavy line. However, for B, the sample can reach wavy line at some of the spanwise positions. As a result, the average wavelength of A is larger than B. That is to say, the increase ratio of the wavelength of transition Zone that has larger curvature radius is relatively high.

In order to calculate the functional relationship between curvature radius and wavelength increase ratio, a semi-circle is used to further simplify the interface structure. As shown in Fig. 8, the curvature radius of the semi-circle is denoted by  $R$ . The spanwise positions where the sample can reach wavy line increased when the sample moves from position  $X_1$  to position  $X_2$ . And the increase length is equal to  $2\Delta Y$ . Therefore, the increase ratio can be written as:

$$\varepsilon = 2\Delta Y / \Delta X \quad (3)$$

In this paper, the  $\Delta X$  is equal to 0.02  $D$ .  $D$  is the diameter of nozzle exit. It is easy to calculate that the increasing length  $\Delta Y$  can be written as:

$$\Delta Y = R - \sqrt{R^2 - (\Delta X)^2} \quad (4)$$

Substituting Eq. (3) into Eq. (2) gives the relationship between curvature radius and increase ratio:

$$R = \left(\frac{2}{\varepsilon} + \frac{\varepsilon}{2}\right) \times 10^{-2} D \quad (5)$$

Therefore, the spanwise wavelength is :

$$\lambda_y = 2R = \left(\frac{4}{\varepsilon} + \varepsilon\right) \times 10^{-2} D \quad (6)$$

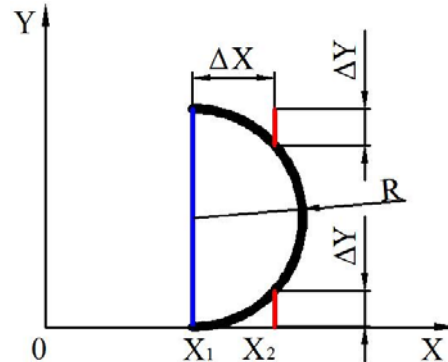


**Fig. 8. Simplified model of interface structure.**

### 2.3 Validation

The accuracy of the Welch method in wavelength measurement is validated here. As presented in the Fig. 9(a), an image of a ruler is used. The distance between two adjacent calibrations is equal to 1 mm which is corresponds to 13 pixels. Along the red line of the Fig. 9(a), the image intensities were extracted and processed with Welch method.

The result is presented in Fig. 9(b). In the range of  $X=0\sim 280$  pixels, the image intensities were extracted from the background which has no explicit order. As a result, the processed wavelengths have

no order and fluctuate from 0 to 0.2 mm. However, in the range of  $X = 280\sim 630$  pixels, the wavelengths are all the same and equal to 0.99 mm. The error of the wavelength measurement is 1%.

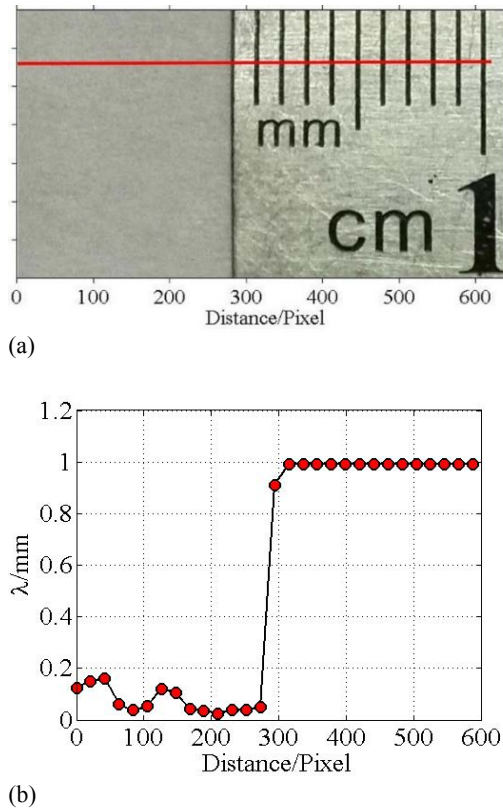


**Fig. 9. Validation of Welch method. (a) Rule image. (b) Processing result.**

The accuracy of spanwise wavelength calculation is validated here. The increase ratio of wavelength of transition Zone in Fig. 5 is around 0.25. According to Eq. (3), the corresponding curvature radius is equal to 0.081 D. As shown in Fig. 10, the red circles are tangent to the interface structure of the jet. Therefore, the curvature radius is equal to the radius of the circle, which is equal to 0.078 D. The deviation between two results is about 4.2%. This error may be partially due to the 0.078 D is obtained from a single image while the 0.081 D obtained from the average result of 100 images.

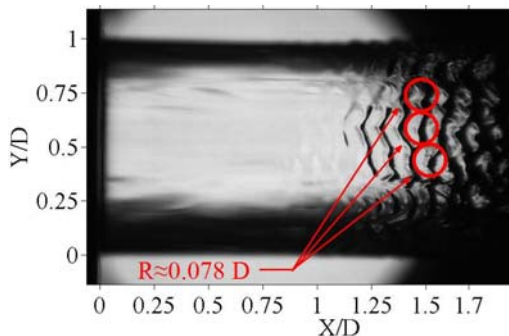


**Fig. 10. Validation of spanwise wavelength. The curvature radius of the red circle is equal to 0.078 D.**

### 3. RESULTS

#### 3.1 Jet Images

Some typical jet images are selected and discussed in the Fig. 11, more jet images of different experimental conditions can be found in the appendix.

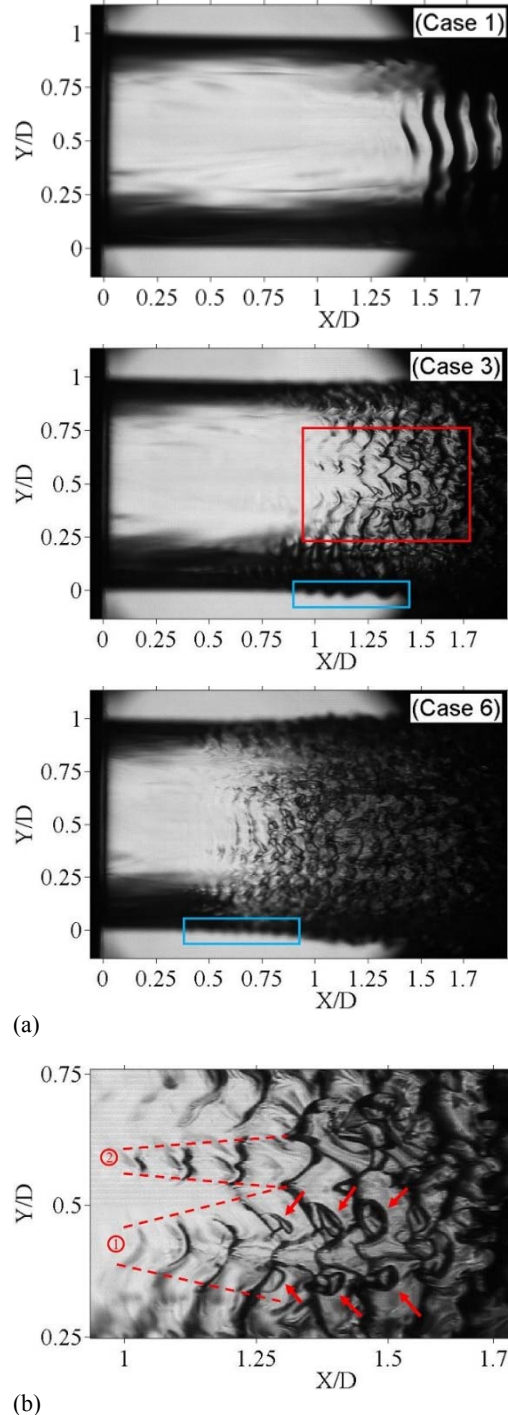


**Fig. 11. Jet images. (a)The Weber numbers of Case 1, Case 3 and Case 6 are 8, 21.1 and 51.9 respectively. The jets of these three Cases are under the first wind-induced breakup regime, second wind-induced breakup regime and atomization regime, respectively.**

Firstly, the jet surface structures of three breakup regimes are compared in the Fig. 11(a). The jet of Case a is under the first wind-induced breakup regime. In the range of  $X/D=0\sim 1.25$ , the jet surface is nearly smooth and there is no clear surface structure. Meanwhile, there is no obvious radial deformation on the left periphery ( $Y/D=0$ ) and right periphery ( $Y/D=0$ ) of the jet. Then, a group of regularly spaced wave-like structures begin to appear on the jet surface at the position of  $X/D=1.4$ . These wave-like structures are defined as surface waves. Under this breakup regime, surface waves are nearly the same in different spanwise and streamwise positions. The streamwise distance of adjacent surface waves is around  $0.1 D$ . The jet of Case c is under the second wind-induced breakup regime. The position where surface waves appear is closer to the nozzle exit. The distance between two adjacent surface waves decrease to  $0.083 D$ . There is clearly radial deformation on the left periphery of the jet (as shown with blue rectangular box). The size of radial deformation increases with streamwise distance. The jet of Case f is under the atomization regime. Compared with the aforementioned jets, the jet has the shortest smooth part which is around  $0.5 D$ . The streamwise distance of adjacent surface waves is only  $0.075 D$ . The radial deformation of the jet periphery is much smaller. In summary, with the increase of Weber number, the generation position of surface waves is closer to the nozzle exit, the distance between two adjacent surface waves get shorter and the size of radial deformation decrease.

In our work, the part between nozzle exit and the position that jet interface wave forms is defined as the smooth part. Obviously, the length of the smooth part is dependent on the generation position of jet interface wave. However, there is no generally accepted explanation for the generation of jet interface wave. One of the explanations was given by Koch (Koch W 1985), he believes that the interface wave is developed from the disturbance whose frequency is equal to the system's most unstable frequency. The disturbance firstly grows inside the absolutely unstable region, then reaches convectively unstable region and forms the interface wave at a streamwise position. Based on the Koch' analysis, the streamwise position is located at  $X/D\sim 3.5 \times 10^{-4}$ , which is significantly far from the measured jet interface wave. The authors believe that our experimental results may be helpful for the future improvement of the related theory.

Secondly, the development of surface waves is discussed with the help of Fig. 11(b). The Fig. 11(b) is the local enlarged image of the Case c (red rectangular box). The surface waves are complicated under this breakup regime. As it is shown in the enlarged image, surface waves are separated and isolated in the spanwise direction at the beginning. With the streamwise distance increased, the surface waves of the two groups expand along the spanwise direction and intersect with each other at the position of  $X/D=1.35$ . The surface waves of group one experience a process of fork-like division. The surface wave divides into two parts at the position of

$X/D=1.4$ . It is worth noting that there are some smaller interface structures (as pointed with the red arrow) appear near the top of the surface waves. In this paper, these smaller surface structures are defined as secondary waves. The researches of Landahl (Landahl 1972) and Hoyt (Hoyt & Taylor 1977a) show that the secondary waves are the results of the development of secondary instability. The hairpin vortex lifting up from the surface downstream of the primary wave crest may responsible for the formation of the secondary waves. The size of secondary waves is getting bigger with the increase of streamwise distance. From the position of  $X/D=1.4$  to the further downstream, the surface structures became disordered. Based on the above analysis, it can be concluded that the interaction of the surface waves of different spanwise positions, the division of the surface waves and the generation of secondary waves and their interaction with surface waves are responsible for the transition of periodic surface waves into disordered surface structures.

### 3.2 Streamwise Wavelength of Interface Structure

In Fig. 5, the wavelength curve is divided into three zones, which are smooth Zone (Zone 1), transition Zone (Zone 2) and unsmooth Zone (Zone 3). The curves in Fig. 12 are corresponding to the unsmooth Zones of different Weber number. Several trends can be concluded from this figure. Firstly, under the same Weber number, wavelength generally increases with a same ratio along the streamwise direction. Secondly, the ratio slightly increases with the Weber number increases. Thirdly, for the different Weber numbers, the wavelengths decrease significantly with Weber number.

A possible reason is responsible for the first trend. The velocity of jet surface is zero at the nozzle exit due to the inertia. There must be a velocity gradient between jet surface and jet core. Therefore, the jet surface is supposed to accelerate as the jet move downstream. The acceleration of jet interface and the relaxation of the velocity profile of the liquid jet result in the increases of jet interface wave (Goldstein S 1933; Sato & Kuriki 1961; Brennen C 1970).

The second trend can also be explained by the velocity different between jet core and jet surface. The increase of Weber number indicates the increase of jet core. Accordingly, the velocity gradient between jet surface and jet core will increase. This may lead to the increase of the ratio.

The reason of the thirdly trend could be explained with the work of McCarthy & Molloy (1974) and Park & Heister (2006). The research of McCarthy suggested that the vorticity convect downstream from the boundary layer plays an important role in determining the wavelength. Park's work shows that the thicker boundary layer is corresponding to a stronger vortex and larger wavelength. The boundary layer thickness is inversely proportional to the jet velocity. As a result, the streamwise wavelength of smaller Weber number is bigger.

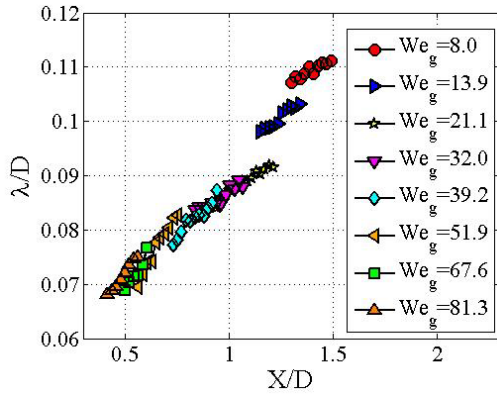


Fig. 12. Variation of streamwise wavelengths.

### 3.3 Spanwise Wavelength of Interface Structure

The transition Zones of eight different Weber numbers are presented in Fig. 13. The results show that these transition Zones have similar trends, and the increase ratios are nearly the same. Based on the analysis above, it can be concluded that the interface structures of different Weber numbers have similar curvature radii. In other words, the spanwise wavelength of the interface structure is not sensitive to the Weber number.

Marmottant & Villermaux' work (2004) shows that spanwise wavelength is dependent on surface tension and is inversely proportional to the gas velocity. In our experiment, the surface tension and gas velocity are constants. As a result, the spanwise wavelengths of different Weber numbers are constants.

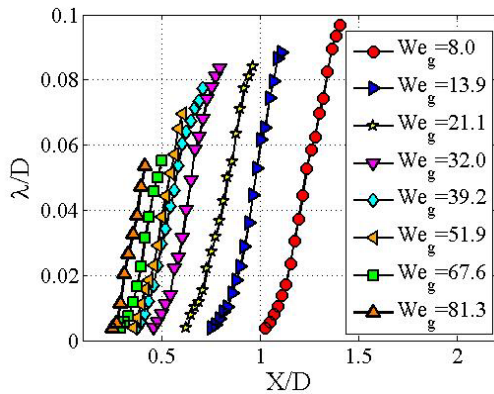


Fig. 13. The transition Zones of different Weber numbers.

### 3.4 Generation Position of Interface Structure

Based on Fig. 13, the average generation positions and their fitting curve are calculated and presented in Fig. 14. Fig. 14 shows that average generation position decreases exponentially with Weber number. The calculated fitting curve is denoted by:

$$X/D = 3.28 \times We_g^{-0.27} - 0.67 \quad (5)$$

The study of Lasheras & Hopfinger (2000),

Marmottant and Villermaux (2004) shows that the transition position is partially related to the balance between aerodynamic pressure ( $\rho_g \Delta u^2$ ) and capillary pressure ( $\sigma/D$ ), where  $\Delta u$  is velocity of the interface between jet and air. Aerodynamic pressure may serve as a force to introduce the instability of jet surface while the capillary pressure restrains the deformation of the jet surface. At the nozzle exit, the velocity of jet surface is nearly zero, therefore, the capillary pressure plays a leading role and there is no clear deformation on the jet surface. However, the velocity of jet surface will increase with the streamwise distance. As a result, the effect of aerodynamic pressure will become more and more important. And the capillary pressure finally cannot restrain the deformation of the jet surface at some streamwise position. The velocity gradient between jet surface and jet core has an important effect on the increase ratio of jet velocity. Apparently, the larger the Weber numbers the higher the velocity increase ratio. This may partially explain why average transition position is getting close to the nozzle exit as Weber number increases.

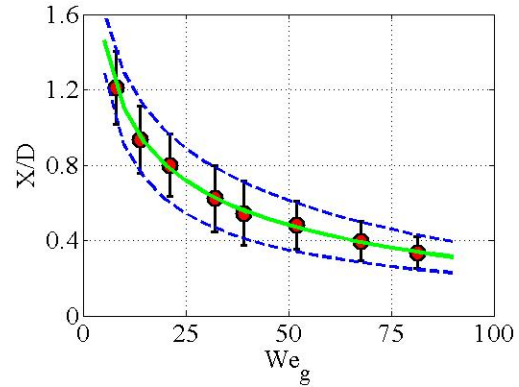


Fig. 14. Average generation position against Weber number. Red circles correspond to the average generation positions. The error bars correspond to upper and lower bounds of the transition region. The green solid line and blue dashed lines are the corresponding fitting curves. For streamwise locations below the lower bound of the transition region, the jet interface is smooth, while for locations above the upper bound, the jet interface enters the unsmooth region.

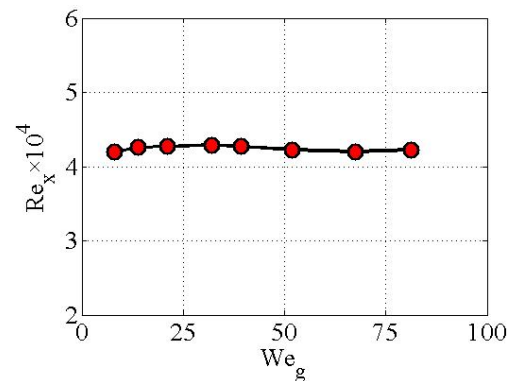
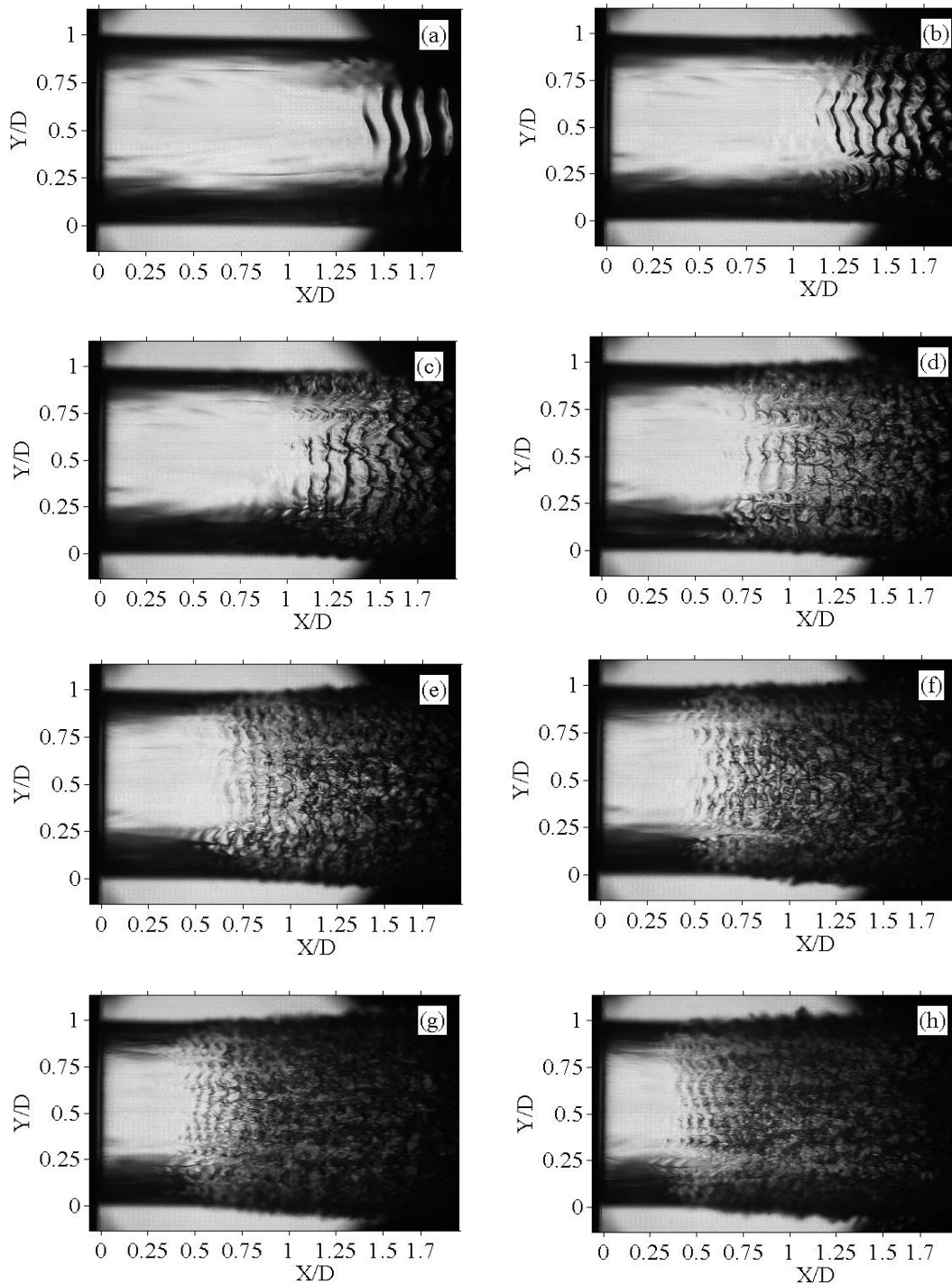


Fig. 15. The variation of  $Re_x$  with Weber number.



**Fig. 16. Evolution of instability waves with increasing Weber numbers.**

As presented in Fig. 14, the average generation position where jet interface translates from smooth to non-smooth varies with Weber number. In order to find a more general regularity of the average generation position, we try to use a non-dimensional parameter to represent it. Therefore, a Reynolds number is defined to estimate the generation of the interface structure. In this paper, the air density, surface tension and nozzle diameter are constants. As a result, Weber number varies only with jet velocity. Therefore, the average transition positions are, in fact,

sensitive to jet velocity. The Reynolds number  $Re_x = \frac{Ux}{\nu}$  that based on the streamwise distance, jet velocity and viscosity is used to characterize the transition of the jet surface. As presented in Fig. 15, all the data are nearly located on the one straight line. As a result, we obtain the average critical Reynolds number ( $Re_x = 4.2 \times 10^4$ ) for all the experimental conditions in this paper. A similar Reynolds number that based on the streamwise distance has already been used in the analysis of the flat-plate boundary layer (Schlichting 1979).

#### 4. CONCLUSIONS

The interface structure of liquid jet is captured and measured with high-speed photography and Welch method respectively. The important parameters of the interface structure are investigated. Main conclusions drawn from this study are as follow:

The jet interface is featured by a group of periodic wave-like structures in the range near the nozzle exit. Along the streamwise direction, the streamwise wavelength of these interface structures generally increases with a same ratio. With the Weber number increase, the ratio slightly increases while the wavelength significantly decreases.

The position where jet surface translates from smooth to unsmooth fluctuates in a certain region with the variation of times and spanwise positions. The spanwise wavelength is the function of nozzle diameter and the wavelength increase ratio of transition region. For the same nozzle, the spanwise wavelength is a constant.

The average transition position decreases exponentially with Weber number. A Reynolds number that based on the streamwise distance, jet velocity and viscosity was proposed to estimate the transition of jet interface. With the same nozzle, the Reynolds number keeps constant. In this paper, the Reynolds number is equal to  $4.2 \times 10^4$ .

#### APPENDIX: LIQUID JET IMAGES

The selected jet images of different inlet pressures are presented in the Fig. 16.

#### ACKNOWLEDGEMENTS

The authors gratefully acknowledge the financial support of National Natural Science Foundation of China (Grant Nos. 51176065 and 51475215), a Project Funded by the Priority Academic Program Development of Jiangsu Higher Education Institutions (PAPD), and the Research and Innovation Project for College Graduates of Jiangsu Province (KYLX15\_1069).

#### REFERENCES

- Behzad, M., N. A. Shgrizb and B. W. Karney (2016). Surface breakup of a non-turbulent liquid jet injected into a high pressure gaseous crossflow, *International Journal of Multiphase Flow* 80, 100–117.
- Bian, S., S. L. Ceccio and J. F. Driscoll (2010). A dual-camera cinematographic PIV measurement system at kilohertz frame rate for high-speed unsteady flows. *Experiments in Fluids* 48, 487–495.
- Brennen, C. (1970). Cavity surface wave patterns and general appearance, *Journal of Fluid Mechanics* 44(1), 33.
- Charalampous, G., C. Hadjiyiannis and Y. Hardalupas (2016). Comparative measurement of the breakup length of liquid jets in airblast atomisers using optical connectivity, electrical connectivity and shadowgraphy. *Measurement* 89, 288–299.
- Cousin, J., A. Berlemont, T. Ménard and S. Grout (2012). Primary breakup simulation of a liquid jet discharged by a low-pressure compound nozzle, *Computers and Fluids* 63, 165–173.
- Desjardins, O., J. O. McCaslin, M. Owkes and P. Brady (2013). Direct numerical and large-eddy simulation of primary atomization in complex geometries, *Atomization and Sprays* 23(11), 1001–1048.
- Dumouchel, C., J. B. Blaisot, E. Bouche and *et al.* (2015). Multi-scale analysis of atomizing liquid ligaments. *International Journal of Multiphase Flow* 73, 251–263.
- Eggers, J. and E. Villermaux (2008). Physics of liquid jets. Reports on Progress in Physics 71, 036601.
- Faeth, G. M. and L. P. Hsiang (1995). Structure and breakup properties of sprays. *International Journal of Multiphase Flow* 21, 99–127.
- Ghiji, M., L. Goldsworthy and P. A. Brandner (2016). Numerical and experimental investigation of early stage diesel sprays. *Fuel* 175, 274–286.
- Goldstein, S. (1933). Proceedings of the Royal Society of London, Series A 142, 545.
- Gorokhovski, M. and M. Herrmann (2008). Modeling primary atomization. *Annual Review of Fluid Mechanics* 40, 343–366.
- Hori, T. and J. Sakakibara (2004). High-speed scanning stereoscopic PIV for 3D vorticity measurement in liquids. *Measurement Science and Technology* 15, 1067–1078.
- Hoyt, J. W. and J. J. Taylor (1977a). Waves on water jets. *Journal of Fluid Mechanics* 83, 119–127.
- Hoyt, J. W. and J. J. Taylor (1977b). Turbulence structure in a water jet discharging in air. *Physics of Fluids* 20(10), 253–257.
- Joseph, D. D., J. Belanger and G. S. Beavers (1999). Breakup of a liquid drop suddenly exposed to a high-speed airstream by. *International Journal of Multiphase Flow* 25(6-7), 1263–1303.
- Julien D., V. Stéphane and E. Arnaud (2011). Numerical investigations in Rayleigh breakup of round liquid jets with VOF methods. *Computers and Fluids* 50, 10–23.
- Koch, W. (1985). Local instability characteristics and frequency determination of self-excited wake flows, *Journal of Sound and Vibration* 99(1), 53.
- Landahl, M. T. (1972). wave mechanics of breakdown, *Journal of Fluid Mechanics* 56(4), 775.
- Lasheras, J. C. and E. J. Hopfinger (2000). Liquid jet instability and atomization in a coaxial gas

- stream. *Annual Review of Fluid Mechanics*. 32, 275–308.
- Lefebvre, A. (1998). *Atomization and sprays*, New York: Taylor and Francis.
- Marmottant, P. and E. Villermaux (2004). On spray formation. *Journal of Fluid Mechanics* 498, 73–111.
- Mayer, W. O. H. and R. Branam (2004). Atomization characteristics on the surface of a round liquid jet. *Experiments in Fluids* 36, 528–539.
- McCarthy, M. J. and N. A. Molloy (1974). Review of stability of liquid jets and the influence of nozzle design. *Chemical Engineering Journal* 7, 1–20.
- Mehravaran, K. (2013). Direct Simulations of Primary Atomization in Moderate-Speed Diesel Fuel Injection, *International Journal of Materials, Mechanics and Manufacturing* 1(2), 207-209.
- Meier, G. E. A., A. Kliipper and G. Grabitz (1992). The influence of kinematic waves on jet break down. *Experiments in Fluids* 12, 173-180.
- Mulgrew, B., (2002). *Digital signal processing—concepts and applications* 2nd editio., Palgrave Macmillan.
- Osta, A. R., J. Lee, K. A. Sallam and *et al.* (2012). Study of the effects of the injector length/diameter ratio on the surface properties of turbulent liquid jets in still air using X-ray imaging. *International Journal of Multiphase Flow* 38, 87–98.
- Park, H. and S. D. Heister (2006). A numerical study of primary instability on viscous high-speed jets. *Computers and Fluids* 35(10), 1033–1045.
- Pohlhausen, K. (1921). Zur näherungsweise Integration der Differentialgleichung der laminaren Grenzschicht, *ZAMM* 1(4), 252.
- Reddemann, M. A., F. Mathieu and R. Kneer (2013). Transmitted light microscopy for visualizing the turbulent primary breakup of a microscale liquid jet. *Experiment in Fluids* 54, 1607-1616.
- Sallam, K. A., Z. Dai and G. M. Faeth (1999). Drop formation at the surface of plane turbulent liquid jets in still gases. *International Journal of Multiphase Flow* 25(6), 1161–1180.
- Sallam, K. A., Z. Dai and G. M. Faeth (2002). Liquid breakup at the surface of turbulent round liquid jets in still gases. *International Journal of Multiphase Flow* 28(3), 427–449.
- Sato, H. and K. Kuriki (1961). The mechanism of transition in the wake of a thin flat plate placed parallel to a uniform flow, *Journal of Fluid Mechanics* 11(3), 321.
- Schlichting, H. (1979). *Boundary-Layer Theory.*, 7th ed., McGraw Hill, New York, U.S.A.
- Syuto, T. and *et al.* (2010). Flow visualization and scanning PIV measurement of three-dimensional structure in near field of strongly buoyant jet. *Journal of Visualization* 13, 203–211.
- Tian, X. S., H. Zhao, H. F. Liu and *et al.* (2015). Three-dimensional large eddy simulation of round liquid jet primary breakup in coaxial gas flow using the VOF method. *Fuel Processing Technology* 131, 396–402.
- Tryggvason, W. S. (2000). *Fluid dynamics and transport of droplets and sprays* 2nd ed., Cambridge University Press.
- Umemura, A. (2011). Self-destabilizing mechanism of a laminar inviscid liquid jet issuing from a circular nozzle. *Physical Review E* 83, 046307.
- Umemura, A. (2014). Model for the initiation of atomization in a high-speed laminar liquid jet. *Journal of Fluid Mechanics* 757, 665-700.
- Wu, P. K. and G. M. Faeth (1993). Aerodynamic effects on primary breakup of turbulent liquids. *Atomization and Sprays* 3(3), 265–289.
- Wu, P. K., R. F. Miranda and G. M. Faeth (1995). Effects of initial flow conditions on primary breakup of nonturbulent and turbulent round liquid jets. *Atomization and Sprays* 5(2), 175–196.
- Wu, P. K., L. K. Tseng and G. M. Faeth (1992). Primary breakup in gas/liquid mixing layers for turbulent liquids. *Atomization and Sprays* 2(3), 295–317.
- Xiao, F., M. Dianat and J. J. McGuirk (2014). LES of turbulent liquid jet primary breakup in turbulent coaxial air flow. *International Journal of Multiphase Flow* 60, 103–118.
- Xiao, F., Z. G. Wang and M. B. Sun (2016). Large eddy simulation of liquid jet primary breakup in supersonic air crossflow. *International Journal of Multiphase Flow* 87, 229–240.
- Yecko, P., S. Zaleski, and J. M. Fullana (2002). Viscous modes in two-phase mixing layers. *Physics of Fluids* 14, 4115–4122.
- Yecko, S. and S. Zaleski (2005). Transient growth in two-phase mixing layers. *Journal of Fluid Mechanics* 528, 43–52.
- Yoon, S. S. and S. D. Heister (2004). A fully non-linear model for atomization of high-speed jets. *Engineering Analysis with Boundary Elements* 28(4), 345–357.
- Yoon, S. S. (2003). Categorizing linear theories for atomizing round jets. *Atomization and Sprays* 13(5-6), 499–516.
- Zhao, H., J. L. Xu, J. H. Wu and *et al.* (2015). Breakup morphology of annular liquid sheet with an inner round air stream. *Chemical Engineering Science* 137, 412–422.
- ZhaoH., H. F. Liu, X. S. Tian and *et al.* (2014). Outer ligament-mediated spray formation of annular liquid sheet by an inner round air stream. *Experiment in Fluids* 55, 1793-1805.

